High Quantum Yield Shortwave Infrared Luminescent Tracers for Improved Sorting of Plastic Waste

Krishnan Rajagopalan,* Eduard Madirov, Dmitry Busko, Ian A. Howard, Bryce S. Richards, Hendrik C. Swart, and Andrey Turshatov*

ABSTRACT: More complete recycling of plastic waste is possible only if new technologies that go beyond state-of-the-art near-infrared (NIR) sorting are developed. For example, tracer-based sorting is a new technology that explores the upconversion or down-shift luminescence of special tracers based on inorganic materials codoped with lanthanide ions. Specifically, down-shift tracers emit in the shortwave infrared (SWIR) spectral range and can be detected using a SWIR camera preinstalled in a state-of-the-art sorting machine for NIR sorting. In this study, we synthesized a very efficient SWIR tracer by codoping $Li_3Ba_2Gd_3(MoO_4)_8$ with Yb^{3+} and Er^{3+}, where Yb^{3+} is a synthesizer ion (excited near 976 nm) and Er^{3+} emits near 1550 nm. Fine-tuning of the doping concentration resulted in a tracer $(Li_3Ba_2Gd_{(3-x-y)})(MoO_4)_8$:$xYb^{3+}$, yEr^{3+}, where $x = 0.2$ and $y = 0.4$) with a high photoluminescence quantum yield for 1550 nm emission of 70% (using 976 nm excitation). This tracer was used to mark plastic objects. When the object was illuminated by a halogen lamp and a 976 nm laser, the three parts could be easily distinguished based on reflectance and luminescence spectra in the SWIR range: a plastic bottle made of polyethylene terephthalate, a bottle cap made of high-density polyethylene, and a label made of the tracer $Li_3Ba_2Gd_3(MoO_4)_8$:Yb^{3+}, Er^{3+}. Importantly, the use of the tracer in sorting may require only the installation of a 976 nm laser in a state-of-the-art NIR sorting system.

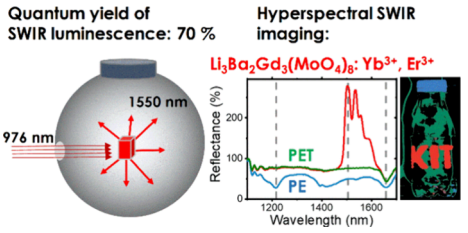

KEYWORDS: *phosphor, molybdate, crystal structure, downshifting, quantum yield, plastic waste recycling*

1. INTRODUCTION

The luminescence of lanthanide (Ln^{3+}) ions is characterized by spectral features with precise excitation and emission peaks as the occupied 5s and 5p orbitals effectively protect the 4f orbitals from the external environment. Owing to these feature properties, Ln^{3+} ions have gained attention in the fields of laser optics,[1,2] light-emitting diodes (LEDs),[3,4] biosensing,[5] bioimaging,[6] anticounterfeiting,[7] photocatalysis,[8] photovoltaics,[9,10] and food safety detection.[11] Plastic recycling is one of the more recent applications of phosphors doped with Ln^{3+} ions.[12] In 2021, more than 29 million tons of postconsumer plastic waste were collected in the European Union (EU). Of this waste stream, only 35% is recycled, 42% is reprocessed for energy, and 23% is dumped into landfills (although, over the past 15 years, landfill disposal has decreased significantly).[13] At the same time, only 9.9% of Europe's total demand for plastic, some 55.6 million tons, is covered by recycled polymers, creating a huge obstacle in realizing a circular economy.[13] In 2018, the EU adopted ambitious targets: to increase the reuse and recycling of plastic waste to 50% by 2025 and 55% by 2030.[14] With the state-of-the-art near-infrared (NIR) sorting technology, packaging waste can only be sorted according to the main polymers—polyolefins, polyethylenterephthalat (PET), polystyrene, and polyvinyl chloride.[15] However, full recycling is only possible by differentiating by specification, such as PET for food applications (trays) versus nonfood applications (personal care), or even by brand. Sorting technologies that can achieve this differentiation are still under development.

The core measurement behind NIR sorting is a comparison of the reflectance spectra of plastics in the 1000−1700 nm range under halogen lamp illumination. Importantly, a new sorting technology, tracer-based sorting (TBS), can be implemented on existing sorters without complex upgrades. To improve the quality of plastic sorting based on NIR reflectance, optical signatures from luminescent tracers, either doped into the bulk polymer or applied via a printed label, can be used.[16] Further away, several different sorting codes should be established to increase the palette of sorted materials with similar reflectance spectra.[17] Here, Ln^{3+} luminescence with distinct and narrow emission spectra over a wide spectral range, from ultraviolet (UV) to shortwave infrared (SWIR; 1000−2000 nm), can provide an excellent solution for the TBS process. In particular, detection of Ln^{3+} luminescence in the spectral range where state-of-the-art SWIR sorting machines

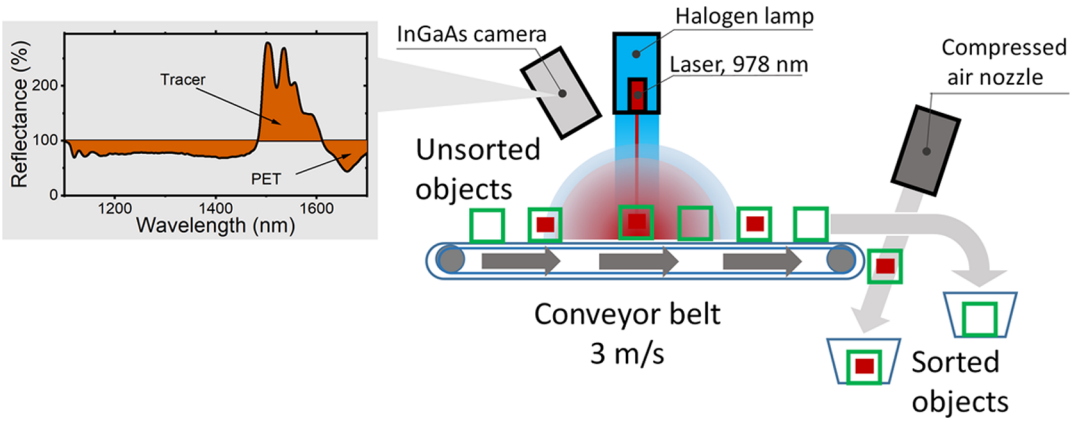

Figure 1. Schematic of an NIR sorting machine equipped with a 978 nm laser. The InGaAs camera measures the reflectance (R) of objects (where absorption contributes as signal $R < 100\%$, while luminescence contributes as $R > 100\%$), while the conveyor belt moves at a speed of up to 3 m/s. For example, under simultaneous illumination with a halogen lamp and a 978 nm laser, the absorption peak of polyethylene terephthalate contributes to the minimum at 1630−1700 nm and the luminescence of Er^{3+} from a tracer contributes as a peak at 1460−1630 nm. Thus, among all PET objects, objects carrying an additional tracer can be identified and sorted out by compressed air.

operate can increase the sorting quality and provide additional economic benefits by combining new and already established technologies (Figure 1). Ions such as Er^{3+}, Tm^{3+}, and Ho^{3+} have emission peaks in the SWIR at 1450−1650, 1700−1900, and 1150−1250 nm, respectively. All of these Ln^{3+} ions are characterized by a rather small absorption cross section, which results in a low emission signal and usually causes an increase in the required marker concentration on a label. For this reason, the Yb^{3+} ion, which has the highest absorption cross section in a Ln^{3+} series, is typically used as a sensitizer, while other doping ions serve as activators and benefit from the energy absorbed by Yb^{3+}.

Although the energy of optical 4f−4f transitions in Ln^{3+} ions shows weak sensitivity to the environment, their radiative properties, a rate of radiative transitions and luminescence quantum yield (PLQY), are sensitive enough to the surrounding crystal field and provide plenty of opportunities for tuning when different inorganic crystal hosts are employed. Among inorganic phosphors, molybdate hosts generally have many attractive features, including easy solid-state growth and synthesis of the compounds with high Ln^{3+} doping content.[18−20] Furthermore, ternary molybdates with the structural formula $Li_3Ba_2Ln_3(MoO_4)_8$ have garnered considerable attention in recent years because they exhibit a large amount of structural diversity combined with outstanding thermal and chemical stability, a high degree of crystallinity, and a moderate phonon energy of approximately 1000 cm^{-1}.[21−23] The family of ternary cationic molybdates $Li_3Ba_2Ln_3(MoO_4)_8$ was initially reported by Klevtsova et al.,[24] and García-Cortés et al.[23] They explained that partial replacement of the Ln^{3+}, Ba^{2+}, and Li^+ cations in the ternary molybdate system makes it possible to construct a wide variety of structures with more complex compositions. In the ternary cationic molybdate system, there is no inversion center geometry at either the Ba^{2+} or Gd^{3+} site, which are connected by five and eight O^{2-} ions, respectively. Specifically, two crystal point locations for Ln^{3+} with significantly distinct symmetries (8f and 4e) were reported in this $Li_3Ba_2Ln_3(MoO_4)_8$ system.[23] The degree of distortion around these Ln^{3+} crystal sites is rather significant, which is possibly evidence of a strong crystal field interaction around the 8f and 4e sites, making them an excellent phosphor candidate. Mo^{6+} ions are located at different 8f general locations over two separate sites (Mo1, Mo2), with coordination from oxygen ions to create significantly distorted tetrahedral surroundings.[22,25] This causes a spatially disordered environment surrounding the Ln^{3+} dopant ions, resulting in an inhomogeneous broadening of the spectral peaks.[26,27]

The outstanding luminescence performance of Eu^{3+}-doped $Li_3Ba_2La_3(MoO_4)_8$ was demonstrated by Katelnikovas et al.[28] Under 465 nm excitation, these materials (with variable concentrations of Eu^{3+}) demonstrated a PLQY of nearly 100%. The remarkable advantage of ternary molybdate systems in achieving high Ln^{3+} ion doping without concentration quenching was also recently demonstrated.[21,28−30] In addition, the incorporation of high concentrations of Ln^{3+} ions increases the absorption cross section, resulting in brighter luminescence.[27] The $Li_3Ba_2Y_3(MoO_4)_8:Yb^{3+}$,[31] $Li_3Ba_2La_3(MoO_4)_8:Dy^{3+}$,[32] $Li_3Ba_2Y_3(MoO_4)_8:Er^{3+}$,[2] and $Li_3Ba_2Nd_3(MoO_4)_8$,[33] crystals were reported as being potential candidates for solid-state laser materials, exhibiting both large absorption and emission cross sections. Therefore, this ternary molybdate system with the formula $Li_3Ba_2Ln_3(MoO_4)_8$ has the potential to provide suitable sites for Yb^{3+}/Er^{3+} substitution and is an excellent host if selected for bright Er^{3+} emission in the SWIR region.

When excited in the 940−980 nm range, Yb^{3+}- and Er^{3+}-activated phosphors are expected to emit SWIR luminescence with reasonable efficiency due to energy transfer from Yb^{3+} to Er^{3+} and the Er^{3+}:$^4I_{13/2} \rightarrow {}^4I_{15/2}$ transition with a broad emission band centered at approximately 1530 nm. However, the high doping concentration of Yb^{3+} and Er^{3+} ions in many materials leads to a situation in which the activator Er^{3+} ion transfers most of its energy to another Er^{3+} via energy migration[34] and/or to the sensitizer Yb^{3+} via back energy transfer.[35] As a result, the downshift (DS) emission of Er^{3+} at about 1530 nm is reduced. Fine-tuning of the doping concentrations of Yb^{3+} and Er^{3+} is often required to achieve the strongest luminescence.

Because of its universal applicability, the PLQY has become a critical metric for the objective comparison of the efficacy of different types of luminescent phosphors.[36] It should be noted that absolute PLQY values for Er^{3+} SWIR emission measured directly with an integrating sphere are scarce. Recently, PLQY

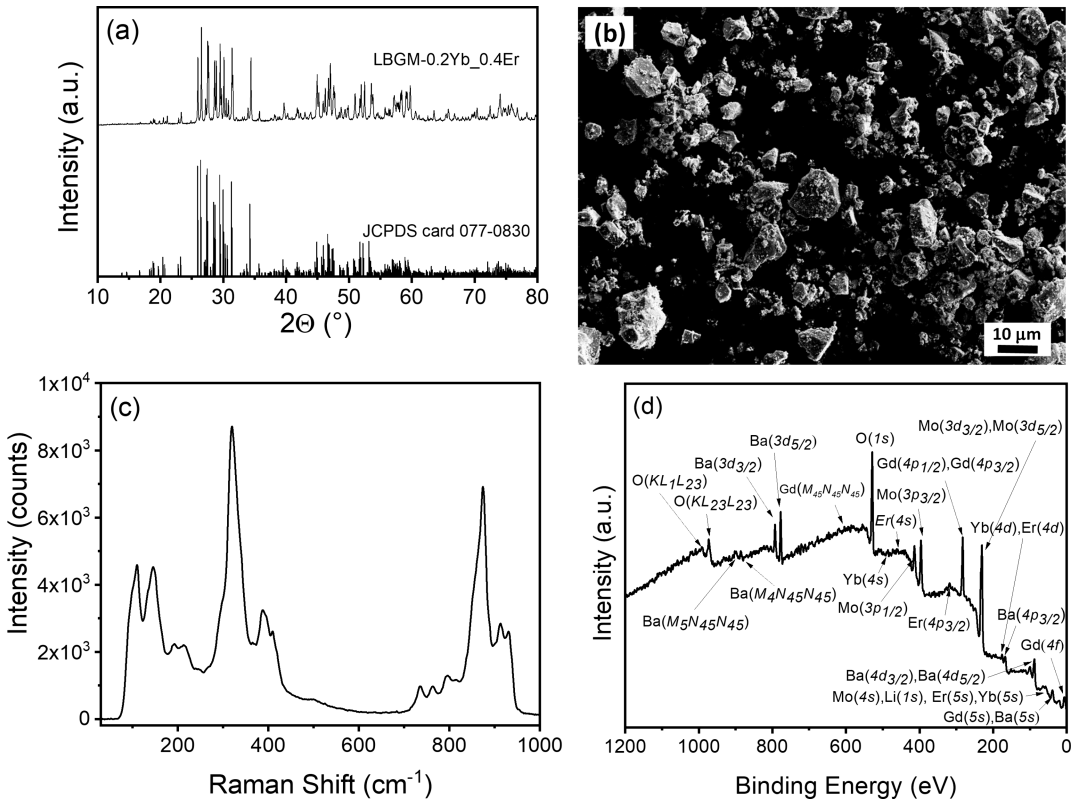

Figure 2. Characterization of the representative LBGM-0.2Yb_0.4Er sample: (a) Powder XRD patterns; (b) SEM image; (c) Raman spectrum of undoped LBGM material; (d) XPS spectrum.

values ranging from 4.3 to 9.3% were reported for the SWIR Er^{3+} emission for a series of perovskite and CaS microcrystals.[37−39] Another example of efficient SWIR luminescence of Er^{3+} was demonstrated for $NaCeF_4$:Er^{3+},Yb^{3+} nanocrystals, which exhibited 1530 nm luminescence with a PLQY = 33% under 980 nm excitation.[40] However, such nanomaterials are usually composed of core/shell/combinatorial structures[41,42] and therefore lengthy synthesis techniques prevent the preparation of the phosphor in a single gram-scale step.[43] Thus, it is critical to develop Er^{3+}/Yb^{3+} ion-doped microcrystalline phosphors that combine simple synthesis with an enhanced quantum yield for SWIR applications.

To address this knowledge gap, the current study appears to address the following two research questions: (i) How does the fine-tuning of the Er^{3+}/Yb^{3+} doping concentration aid in achieving a high PLQY of SWIR luminescence in a $Li_3Ba_2Gd_3(MoO_4)_8$ (LBGM) host? (ii) How does the simultaneous laser (976 nm) and halogen lamp irradiation of plastics with printed LBGM:Yb^{3+},Er^{3+} tracers improve plastic sorting?

To the best of our knowledge, this is the first study to demonstrate the solid-state synthesis of the LBGM phosphor with a focus on enhancing the NIR luminescence at 1530 nm and improving the PLQY by changing the Yb^{3+} and Er^{3+} ion concentrations.

2. RESULTS AND DISCUSSION

2.1. Structural Analysis. Figure 2 provides a summary of the results obtained on a representative sample $Li_3Ba_2Gd_{(3-x-y)}(MoO_4)_8$:$x$$Yb^{3+}$,$y$$Er^{3+}$, where x = 0.2 and y = 0.4 (LBGM-0.2Yb_0.4Er). The XRD results in Figure 2a and Figures S1 and S2 show a perfect monoclinic crystalline phase, with all significant reflections easily indexed from LBGM material with the $C2/c$ space group (JCPDS card 077-0830).[22,24,25,28] High-quality single-phase LBGM phosphors are present, as demonstrated by the intense, narrow peaks in the XRD patterns. All of the XRD patterns showed no indication of any contamination peak, which is a clear sign that Yb^{3+} and Er^{3+} ions were accommodated in the materials replacing Gd^{3+} ions. The incorporation of Yb^{3+} and Er^{3+} ions into the LBGM replacing Gd^{3+} ions caused a slight shift in the peak position toward a high 2θ angle. For instance, the most intense reflection observed at 26.4° corresponds to the plane $(11\bar{4})$ shifted to 26.8° when the doping concentration of Yb^{3+} was increased with a fixed Er^{3+} concentration. A similar trend was also observed when the Er^{3+} ion concentration was changed to a fixed Yb^{3+} concentration or vice versa (Figure S4).

The surface morphology of the LBGM-0.2Yb_0.4Er sample is represented in Figure 2b. SEM analysis revealed that the phosphor was composed of micron-sized particles. The average size of the particles was found to be ∼4−5 μm, and there was also evidence of the existence of larger clusters, with sizes reaching as high as ∼10 μm. These larger clusters are probably consistent agglomerations that originated from strong interactions between the fragments. Energy-dispersive X-ray (EDX) spectroscopy performed for the representative LBGM-0.2Yb_0.4Er sample (Figure S4) shows characteristic peaks for Ba, Gd, Mo, Yb, and Er elements that are located within a microparticle.

Figure 2c shows the room-temperature Raman spectrum obtained for the undoped LBGM powder. This is due to the fact that all samples containing Yb^{3+}/Er^{3+} dopants exhibited an intense signal at >1000 cm^{-1} in the Raman spectrum, which is

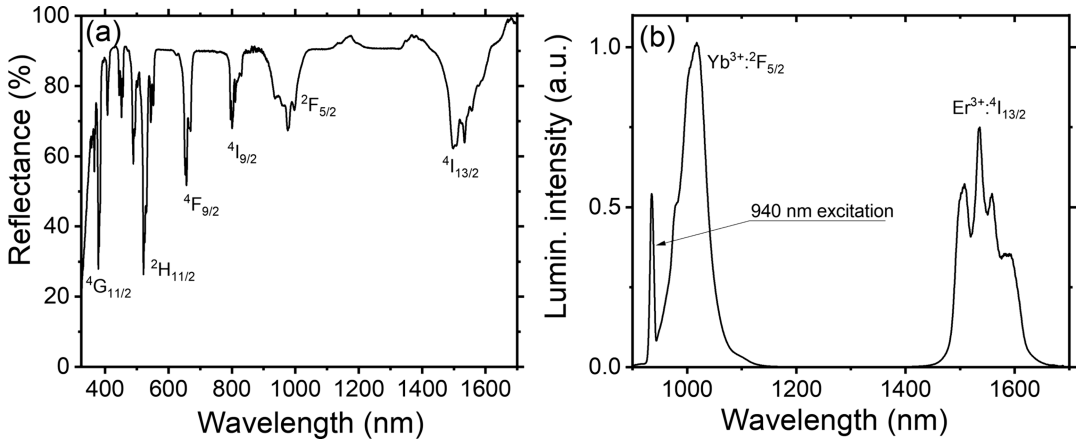

Figure 3. Characterization of the representative LBGM-0.2Yb_0.4Er sample. (a) Diffuse reflection spectrum. (b) Luminescence spectrum under 940 nm laser excitation.

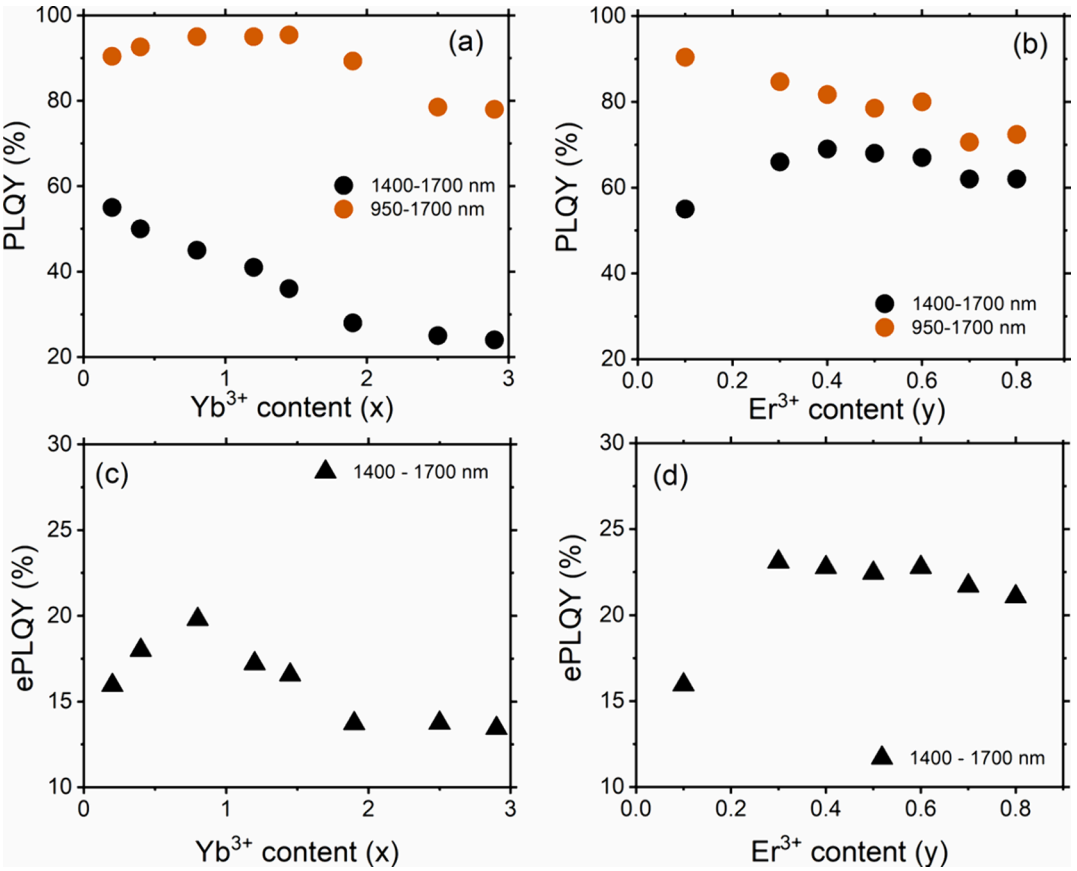

Figure 4. (a, b) Corrected PLQY for the Er^{3+}:$^4I_{13/2}$ → $^4I_{15/2}$ (1400−1700 nm) transition and Yb^{3+}:$^2F_{5/2}$ → $^2F_{7/2}$ + Er^{3+}:$^4I_{13/2}$ → $^4I_{15/2}$ transitions (950−1700 nm) in $Li_3Ba_2Gd_{(3-x-y)}(MoO_4)_8$:$xYb^{3+}$,$yEr^{3+}$ samples. (c, d) ePLQY for the Er^{3+}:$^4I_{13/2}$ → $^4I_{15/2}$ (1400−1700 nm) transition in $Li_3Ba_2Gd_{(3-x-y)}(MoO_4)_8$:$xYb^{3+}$,$yEr^{3+}$ samples.

attributed to Ln^{3+} luminescence, excited by 785 nm laser of the Raman spectrometer. The strong, easily distinguishable bands in the Raman spectrum indicate that the synthesized micrometer-sized particles were in good crystalline form. The Raman spectrum is used to estimate the maximum phonon energy (930 cm^{-1}) of the LBGM host. A more detailed description of the Raman and FTIR spectra can be found in the Figures S5 and S6, respectively.

High-resolution XPS scans were performed to evaluate the chemical states and binding energies of all of the constituents in the LBGM:Yb^{3+},Er^{3+} materials. The occurrence of all of the key chemical components in the as-synthesized material was confirmed by the survey scan XPS spectrum, as illustrated in Figure 2d and Figure S7.

2.2. Optical Properties of $Li_3Ba_2Gd_3(MoO_4)_8$:Yb^{3+},Er^{3+}. All LBGM samples exhibited diffuse reflectance spectra similar to those of the representative LBGM-0.2Yb_0.4Er sample, with typical peaks corresponding to absorption peaks in Er^{3+} and Yb^{3+} ions (Figure 3a). The luminescence of the representative sample LBGM-0.2Yb_0.4Er is shown in Figure

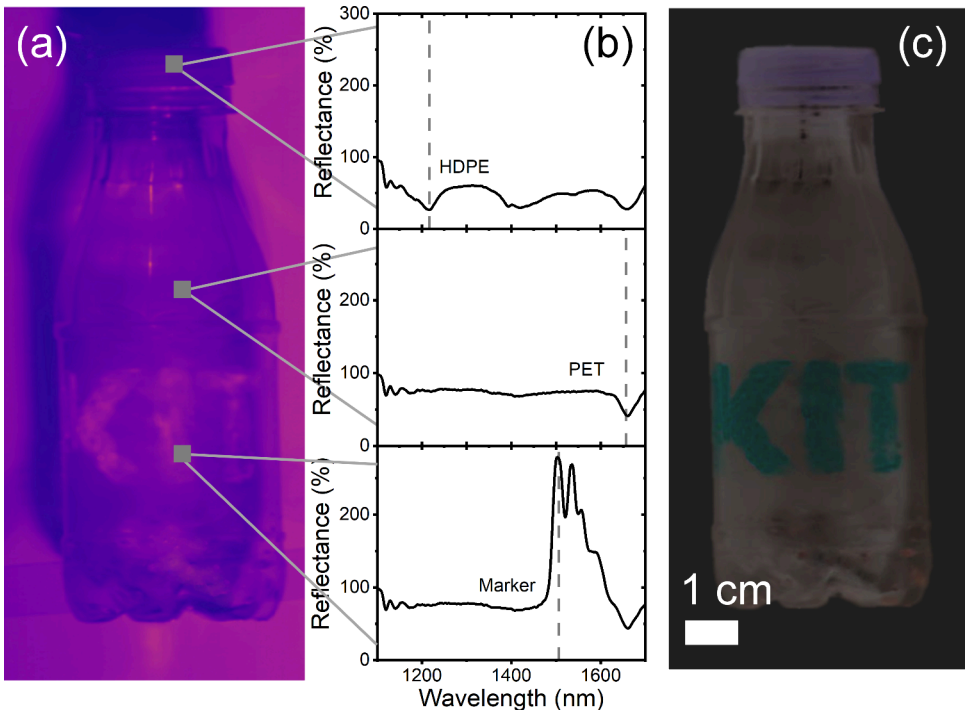

Figure 5. (a) Image of a plastic bottle obtained with a hyperspectral SWIR camera in the intensity measurement regime. A halogen lamp and a 976 nm laser (2 W/cm^2) were used for illumination. Each pixel in the image carries additional spectral information. (b) Reflectance spectra extracted from pixels corresponding to bottle, bottle cap, and label with LBGM:Yb^{3+},Er^{3+} tracer. (c) False-color style classification of objects: bottle (PET, gray), bottle cap (HDPE, violet), and label with LBGM:Yb^{3+},Er^{3+} tracer (green).

3b, whereas the luminescence spectra of the other LBGM samples are shown in Figure S8. All LBGM samples exhibited a 1537 nm peak corresponding to the Er^{3+}:$^4I_{13/2} \rightarrow {}^4I_{15/2}$ transition and a 1012 nm peak corresponding to the Yb^{3+}:$^2F_{5/2} \rightarrow {}^2F_{7/2}$ transition when the samples were excited with a 940 nm laser, as shown in Figure 3b.

Although the choice of the two excitation wavelengths used (940 or 978 nm) is not essential for the PLQY measurements, it should be noted that the 978 nm laser excitation is more important for practical applications because this laser wavelength corresponds to the absorption maximum of Yb^{3+} (Figure 3a), while excitation with a 940 nm laser allows an integration of the luminescence peak of Yb^{3+} (which spans from 950 to 1100 nm) for a more accurate calculation of its DS PLQY.

The results of the PLQY measurements in the integrating sphere for the powder samples are shown in Figure 4 and Figure S9. It should be noted that measurements in the integrating sphere for the powder sample often underestimate the PLQY due to two reasons: (a) reabsorption of luminescence by the sample before the light exits from the sample and (b) reabsorption of luminescence by the sample due to multiple scattering/reflection events on the wall of the integrating sphere. To evaluate these effects, two sets of measurements for the same sample were performed in addition to the integrating sphere measurements: (a) luminescence spectra outside the integrating sphere and (b) luminescence spectra outside the integrating sphere for a diluted powder sample (the dilution was made using an undoped LBGM sample with a mass ratio between doped and undoped samples of 1:9) (Figures S10–S13). The correction of the PLQY considering the reabsorption process was performed as described by Wilson and Richards.[44] Briefly, the long-wavelength tail of the luminescence peak obtained outside the sphere was adjusted to the spectra obtained inside the sphere, and PLQY for a powder sample and a diluted powder sample (both outside the integrating sphere) were calculated using eq 1

$$\mathrm{PLQY} = \frac{\mathrm{PLQY}^s}{1 - a + a \times \mathrm{PLQY}^s} \tag{1}$$

where PLQY^s is a value measured in an integrating sphere, in which $a = 1 - \frac{\int I_0 d\lambda}{\int I_d d\lambda}$ with I_0 is the normalized emission intensity of a sample and I_d is the normalized emission intensity of a 1:9 diluted powder sample. The integration ranges are 920–1100 nm for the {Er^{3+}:$^4I_{11/2}$ and Yb^{3+}:$^2F_{7/2}$} band and 1430–1700 nm for the $^4I_{13/2}$– $^4I_{15/2}$ emission band.

Figures S10–S13 show that only a small part of the emitted photons is absorbed after reflection from a wall of the integrating sphere while a much larger part of the luminescence is absorbed inside the sample before the light leaves the sample. The dilution experiment (with different ratios between doped and undoped powders) shows that the shape of luminescence peaks does not change anymore when the mass of undoped powder exceeds nine parts to one part of the doped sample (Figure S14). The corrected PLQY values (using eq 1) are shown in Figure 4 and Figure S15. Figure 3a demonstrates the PLQY values for samples with a fixed amount of Er^{3+} where the concentration of Yb^{3+} gradually increased. PLQY of the Er^{3+}:$^4I_{13/2} \rightarrow {}^4I_{15/2}$ transition decreases from 55 to 24% with increasing Yb^{3+} concentration. A rather unusual result is shown in Figure S15b; the PLQY of Yb^{3+} emission increases from 36 to 61% with increasing Yb^{3+} concentration and only decreases down to 54% for two samples with the highest Yb^{3+} concentration (LBGM-2.5Yb_0.1Er and LBGM-

2.8Yb_0.1Er). In general, the Yb^{3+}:$^2F_{7/2}$ and Er^{3+}:$^4I_{11/2}$ levels have very similar energy. Thus, their relative amounts are regulated by the rate of direct energy transfer (Yb^{3+}:$^2F_{7/2}$ → Er^{3+}:$^4I_{11/2}$) and the rate of back energy transfer (Er^{3+}:$^4I_{11/2}$ → Yb^{3+}:$^2F_{7/2}$). As a result, as the Yb^{3+} concentration increases, the rate of back energy transfer also increases, resulting in a higher PLQY for Yb^{3+} emission (from the Yb^{3+}:$^2F_{7/2}$ state) and lower PLQY for Er^{3+} emission (from the Er^{3+}:$^4I_{13/2}$ state). The higher Yb^{3+} doping is generally associated with concentration quenching and a lower PLQY, which can also be observed for LBGM-2.5Yb_0.1Er and LBGM-2.8Yb_0.1Er samples.

It is interesting to note that the sum of the PLQYs of Er^{3+}:$^4I_{13/2}$−$^4I_{15/2}$ and Yb^{3+}:$^2F_{5/2}$ → $^2F_{7/2}$ transitions (Figure 4a) for the LBGM-1.45Yb_0.1Er sample is very close to unity (PLQY = 96%). This high value indicates that the LBGM-1.45Yb_0.1Er sample exhibits a very efficient radiative process in the SWIR region with very little contribution from concentration quenching and multiphonon relaxation (MPR) to the ground state. This observation is consistent with the previously observed results on near-unity PLQY for Eu^{3+} emission in the visible region.

Another concentration series shows the effect of the Er^{3+} concentration (Yb^{3+} concentration is fixed) on the PLQY of the Er^{3+}:$^4I_{13/2}$ → $^4I_{15/2}$ and Yb^{3+}:$^2F_{5/2}$ → $^2F_{7/2}$ transitions (Figure 4b and Figure S15d−f). As the Er^{3+} concentration increases, the PLQY of the Yb^{3+}:$^2F_{5/2}$ → $^2F_{7/2}$ transition decreases (from 17 to 10%) due to the enhancement of the direct energy transfer with increasing acceptor (Er^{3+}) concentration. The PLQY of the Er^{3+}:$^4I_{13/2}$ → $^4I_{15/2}$ transition also slightly decreased from 70 to 61% with increasing Er^{3+} concentration due to concentration quenching. Overall, the highest PLQY = 70% for the emission in the wavelength range 1450−1500 nm was observed for sample LBGM-0.2Yb_0.4Er. This value is nearly six times higher than the previously reported value measured in an integrating sphere (9.3%) for the CaS:Yb^{3+},Er^{3+} crystals[41] and two times higher than the PLQY in $NaCeF_4$:Yb^{3+},Er^{3+} nanocrystals (32.8%).[42] For a practical application, PLQY is not the only important parameter. A phosphor should have a high PLQY in combination with strong absorption to provide a good external PLQY (ePLQY). In our work, we defined ePLQY (%) as the multiplication of PLQY (%) and absorption (%), both parameters measured in the integrating sphere. Figure 4c,d demonstrates that the highest brightness is observed for samples LBGM-0.8Yb_yEr with relatively broad concentration of Er^{3+}-y = 0.3−0.6.

2.3. $Li_3Ba_2Gd_3(MoO_4)_8$:Yb^{3+},Er^{3+} Phosphors for Plastic Sorting. A proof-of-concept application of the SWIR tracer for plastic sorting is shown in Figure 5, which displays an image of a plastic bottle captured using a halogen lamp, a 978 nm laser, and a SWIR hyperspectral camera with characteristics similar to those used in plastic sorting systems. In Figure 4a, each pixel shows the integrated intensity (over the spectral range 1200−1700 nm) of the photons reaching the camera. At the same time, each pixel also carries spectral information—reflectance spectra. For example, a pixel assigned to the bottle has a relatively flat response in the 1200−1630 nm range, with a clear minimum at 1657 nm. This spectral signature corresponds well to the reflectance spectra of polyethylene terephthalate (PET). A pixel assigned to the bottle cap shows a different spectrum with an additional unique minimum at 1217 nm. This feature can be identified as belonging to the reflectance spectra of high-density polyethylene (HDPE). Thus, PET and HDPE can be distinguished and sorted based on their reflectance spectra. However, how can objects made of identical plastic materials (food grade vs nonfood grade plastic or object made by a brand "KIT" vs unknown brand) be sorted? Figure 4 shows the spectrum of a pixel associated with a SWIR LBGM:Yb^{3+},Er^{3+} tracer. The 976 nm laser excites the tracer, which produces strong SWIR luminescence (contributing to the spectrum as a broad peak in the range of 1460−1630 nm with reflectance > 100%). An object carrying such a tracer can be easily identified and sorted out with a feasible modification of an existing sorting system; it requires an installation of a 976 nm laser capable of providing excitation intensity in the range of a few W/cm^2. Figure 4c shows the false-color classification of objects according to the characteristics of their reflectance spectra with well distinguishable (1) bottle, (b) bottle cap, and (3) label. It is worth mentioning that the current concentration of tracer and printing area in Figure 5 is excessive for SWIR luminescence measurement. In practice, much lower concentrations of tracer and labeled area can be used while maintaining a reliable classification.

3. CONCLUSIONS

To sum up, a new luminescent $Li_3Ba_2Gd_3(MoO_4)_8$:Yb^{3+},Er^{3+} tracer with an excellent shortwave infrared photoluminescence quantum yield of 70% was found after optimization of the concentrations of Yb^{3+} and Er^{3+} in the high-temperature solid-state synthesis of the $Li_3Ba_2Gd_3(MoO_4)_8$ host. To demonstrate its practical application, the tracer was successfully applied to PET plastic bottles, where its shortwave infrared photoluminescence could be easily detected by a hyperspectral camera in conjunction with the reflectance spectra of the plastic. Moreover, when used for plastic sorting, the integration of this tracer requires only one modification to the existing state-of-the-art sorting equipment: the installation of a 976 nm laser. This addition allows for reliable identification of both plastic and the tracer. This proposed enhancement to the plastic sorting process provides a valuable method of separating plastics based on specific requirements, such as distinguishing between PET for food applications (trays) and PET for nonfood applications (personal care), or even distinguishing between different brands. As a result, this advancement offers a promising solution for optimizing plastic waste recycling.

4. EXPERIMENTAL PART

4.1. Solid-State Synthesis of $Li_3Ba_2Gd_{(3-x-y)}(MoO_4)_8$:$xEr^{3+}$,$yYb^{3+}$ Phosphors. The $Li_3Ba_2Gd_3(MoO_4)_8$ microsized luminescent phosphor powders were obtained by a typical high-temperature solid-state synthesis procedure. By variation of the doping concentrations of Yb^{3+} and Er^{3+} ions, a series of $Li_3Ba_2Gd_3(MoO_4)_8$ phosphor materials were synthesized by replacing Gd^{3+} ions. The starting materials of Li_2CO_3, $BaCO_3$, Gd_2O_3, MoO_3, Yb_2O_3, and Er_2O_3 were all purchased from Sigma-Aldrich (99.9% purity). The stoichiometric proportions of all the oxide ingredients were placed in an agate mortar and pestle, mixed well, and ground. The raw material blends were then shifted to cylindrical ceramic crucibles and annealed at 800 °C for 3 h in a high-temperature furnace (Thermconcept, KLS-05/11). In the final step, the samples were remilled using an agate mortar pestle before they were analyzed. To explore DS luminescence properties in $Li_3Ba_2Gd_{(3-x-y)}(MoO_4)_8$:$xEr^{3+}$,$yYb^{3+}$ and to achieve the high PLQY initially, we fixed x = 0.1 for the Er^{3+} ion concentration and varied the Yb^{3+} ion concentrations (y = 0.20, 0.40, 0.80, 1.20, 1.45, 1.90, 2.50,

2.90, respectively). To explore further, we maintained the y = 0.20 mol Yb^{3+} ion concentration and changed the Er^{3+} concentrations (x = 0.20, 0.30, 0.40, 0.50, 0.60, 0.70, 0.80).

4.2. Structural Characterization of Samples. To identify the crystallographic phase, a powder diffractometer (Bruker, D8 DISCOVER) was used to collect X-ray diffraction (XRD) patterns from the as-synthesized materials throughout the range of 10 to 80°. The particle size, sample surface morphology, and EDX analyses were performed using an ambient scanning electron microscope (SEM) (Zeiss, SUPRA 60VP) equipped with an SE-II detector. The samples were sputter coated with a thin layer of silver to aid SEM imaging. EDX spectroscopy was performed using a Bruker AXS XFlash Detector 5010 and an accelerating voltage of 10 kV.

High-resolution and survey scans for X-ray photoelectron spectroscopy (XPS) were carried out with the dynamic scanning X-ray photoelectron microprobe (PHI Quantes), having a pass energy of 280 eV, energy steps of 1 eV each increment, and a dwell duration of 50 ms/step for each energy step. The XPS Peak 4.1 program was employed to perform the functions of peak fitting and evaluation of the XPS scans. The Raman spectrum of an undoped $Li_3Ba_2Gd_3(MoO_4)_8$ sample was recorded using 785 nm excitation and with a 3.5 cm^{-1} resolution (Polytec, i-Raman instrument). The FTIR spectrum of the undoped $Li_3Ba_2Gd_3(MoO_4)_8$ sample was recorded using a Vertex 70 (Bruker) spectrometer equipped with an attenuated total reflection sample holder.

4.3. Optical Characterization of Samples. The diffuse reflectance spectra (DRS) and the absorbance spectra of the samples were obtained using a UV/vis/NIR spectrophotometer (PerkinElmer, Lambda 950) equipped with an integrating sphere.

The PLQY value, a metric defined as the ratio of the number of emitted photons to the number of photons absorbed by a sample, was determined using a custom-built optical setup based around an integrating sphere (Labsphere, Ø 6″, 3P-LPM-060-SL). The sample was placed in the middle of a sphere and excited with a continuous-wave laser diode operating at 940 nm (Thorlabs, M9-940-0200). The laser diode was mounted on a temperature-controlled mount (Thorlabs, TCLDM9) and driven with a laser diode controller (Thorlabs, ITC4001). The Er^{3+}:$^4I_{13/2} \rightarrow {}^4I_{15/2}$ and Yb^{3+}:$^2F_{5/2} \rightarrow {}^2F_{7/2}$ luminescence were measured using an NIR spectrometer (Ocean Insight, NIRQuest). The same spectrometer was used to detect both the emission spectrum of the sample and the excitation laser intensity. To reduce the intensity of the excitation wavelength during the measurement of the emission, a 980 nm long-pass filter (Semrock, LP02-980RE-25) was placed between the output port of the integrating sphere and the collecting optical fiber. The PLQY was calculated using the 3M method.[45]

The spectrometer was irradiance calibrated along with the integrating sphere and optical fiber by using an irradiance calibration lamp (Ocean Insight, HL-3plus-INT-CAL-EXT).

A quartz wedge (reflection ∼4%) was used to reflect a fraction of the laser beam onto a silicon photodiode power sensor (Thorlabs, S121C). The power of the excitation laser was monitored with a power meter (Thorlabs, PM320E). The beam sizes were determined using a beam profiler (Thorlabs, BP209-IR/M) using a 2σ definition for the semiminor and semimajor axes. The beam area of the 976 nm laser diode was calculated to be 57.4 × 10^{-3} cm^2. The beam area of the unfocused 940 nm laser was 88.5 × 10^{-3} cm^2.

To obtain the intensity-dependent PLQY, the same setup and measurement techniques were used at each excitation intensity ranging from 0.04 to 2 W/cm^2. The power of the incident laser light was varied with a neutral density (ND) filter wheel (Thorlabs, NDC-100C-2) attached to a stepper motor. The whole system was automated and controlled with custom software developed in-house using the LabVIEW environment.

4.4. Optical Characterization of the Plastic Bottle. The label was prepared by dispersing 25 mg of the LBGM-0.2Yb_0.4Er particles in 2.5 g of transparent nail polish to achieve 10,000 ppm concentration. The bottle was then labeled with a dispersed tracer using the nail polish.

The SWIR image of the plastic bottle was obtained as follows: The bottle was placed on a moving platform, and data was acquired using a hyperspectral camera (Specim, FX17). The sample was illuminated with two light sources—a 150 W halogen lamp (Elro, HL150) and a 978 nm fiber laser (CNI Laser, FC-W-980H) with an intensity of 3.3 W/cm^2. The sample was scanned at a rate of (2 cm/s). The integration time for a frame was set to 20 ms. The process was controlled using in-house-developed software. Reflectance spectra were obtained by dividing the spectra in each pixel by the reference spectrum of a white calibration tile (Specim, OPRS 200.25.10).

AUTHOR INFORMATION

Corresponding Authors

Krishnan Rajagopalan − *Institute of Microstructure Technology, Karlsruhe Institute of Technology, 76344 Eggenstein-Leopoldshafen, Germany; Department of Physics, University of the Free State, Bloemfontein 9300, South Africa;* orcid.org/0000-0002-0214-4599; Email: krishnanrphy@gmail.com

Andrey Turshatov − *Institute of Microstructure Technology, Karlsruhe Institute of Technology, 76344 Eggenstein-Leopoldshafen, Germany;* orcid.org/0000-0002-8004-098X; Email: andrey.turshatov@kit.edu

Authors

Eduard Madirov − *Institute of Microstructure Technology, Karlsruhe Institute of Technology, 76344 Eggenstein-Leopoldshafen, Germany*

Dmitry Busko − *Institute of Microstructure Technology, Karlsruhe Institute of Technology, 76344 Eggenstein-Leopoldshafen, Germany*

Ian A. Howard − *Institute of Microstructure Technology, Karlsruhe Institute of Technology, 76344 Eggenstein-Leopoldshafen, Germany; Light Technology Institute, Karlsruhe Institute of Technology, 76131 Karlsruhe, Germany;* orcid.org/0000-0002-7327-7356

Bryce S. Richards − *Institute of Microstructure Technology, Karlsruhe Institute of Technology, 76344 Eggenstein-Leopoldshafen, Germany; Light Technology Institute, Karlsruhe Institute of Technology, 76131 Karlsruhe, Germany;* orcid.org/0000-0001-5469-048X

Hendrik C. Swart − *Department of Physics, University of the Free State, Bloemfontein 9300, South Africa;* orcid.org/0000-0001-5233-0130

Notes

The authors declare no competing financial interest.

ACKNOWLEDGMENTS

The financial support provided by the Helmholtz Association is gratefully acknowledged: (i) a Recruitment Initiative Fellowship for B.S.R.; (ii) the funding of chemical synthesis equipment from the Helmholtz Materials Energy Foundry (HEMF); and (iii) Research Field Energy – Program Materials and Technologies for the Energy Transition – Topic 1 Photovoltaics. B.S.R. and A.T. acknowledge funding from the EU's Horizon 2020 research and innovation project "Circular Foodpack" – agreement ID 101003806. K.R., H.C.S., I.A.H., and A.T. acknowledge the Deutsche Forschungsgemeinschaft (DFG, German Research Foundation) – agreement no. 453622059. The authors acknowledge Mr. Pascal Wendler (Polysecure GmbH) for conducting hyperspectral imaging. The authors acknowledge Dr. Arzu Ergene for conducting EDX measurements. Dr. Krishnan Rajagopalan's present address is Extreme Light Infrastructure-Nuclear Physics (ELI-NP), "Horia Hulubei" National R&D Institute for Physics and Nuclear Engineering (IFIN-HH), 30 Reactorului Street, 077125 Măgurele, Ilfov, -Romania.

REFERENCES

(1) Yang, Z.; Wang, W.; Pan, J.; Ye, C. Alternating Current Electroluminescent Devices with Inorganic Phosphors for Deformable Displays. *Cell Rep. Phys. Sci.* **2020**, *1* (10), 100213.

(2) Song, M.; Wang, L.; Zhao, M.; Zhang, L.; Wang, G. Optical Spectroscopy, 1.5 Mm Emission and up-Conversion Properties of Er^{3+}-Doped $Li_3Ba_2Gd_3(MoO_4)_8$ Crystal. *J. Lumin.* **2011**, *131* (8), 1571–1576.

(3) Yang, Y.; Li, Y.; Wang, C.; Zhu, C.; Lv, C.; Ma, X.; Yang, D. Rare-Earth Doped ZnO Films: A Material Platform to Realize Multicolor and Near-Infrared Electroluminescence. *Adv. Opt. Mater.* **2014**, *2* (3), 240–244.

(4) Watanabe, N.; Ide, K.; Kim, J.; Katase, T.; Hiramatsu, H.; Hosono, H.; Kamiya, T. Multiple Color Inorganic Thin-Film Phosphor, RE-Doped Amorphous Gallium Oxide (RE= Rare Earth: Pr, Sm, Tb, and Dy), Deposited at Room Temperature. *Phys. status solidi* **2019**, *216* (5), 1700833.

(5) Kim, E. H.; Han, H.; Yu, S.; Park, C.; Kim, G.; Jeong, B.; Lee, S. W.; Kim, J. S.; Lee, S.; Kim, J. Interactive Skin Display with Epidermal Stimuli Electrode. *Adv. Sci.* **2019**, *6* (13), 1802351.

(6) Cheng, X.; Zhou, J.; Yue, J.; Wei, Y.; Gao, C.; Xie, X.; Huang, L. Recent Development in Sensitizers for Lanthanide-Doped upconversion Luminescence. *Chem. Rev.* **2022**, *122* (21), 15998–16050.

(7) Kumar, V.; Gota, F.; Neyret, J.; Katumo, N.; Chauhan, A.; Dottermusch, S.; Richards, B. S.; Howard, I. A. Smartphone Authentication of Unclonable anticounterfeiting Labels Based on a Microlens Array atop a Microphosphor-Doped Layer. *Adv. Mater. Technol.* **2023**, *8* (6), 2201311.

(8) Richards, B. S.; Hudry, D.; Busko, D.; Turshatov, A.; Howard, I. A. Photon upconversion for Photovoltaics and Photocatalysis: A Critical Review: Focus Review. *Chem. Rev.* **2021**, *121* (15), 9165–9195.

(9) Lee, K.-T.; Park, J.-H.; Kwon, S. J.; Kwon, H.-K.; Kyhm, J.; Kwak, K.-W.; Jang, H. S.; Kim, S. Y.; Han, J. S.; Lee, S.-H. Simultaneous Enhancement of upconversion and Downshifting Luminescence via Plasmonic Structure. *Nano Lett.* **2015**, *15* (4), 2491–2497.

(10) Singh, R.; Madirov, E.; Busko, D.; Hossain, I. M.; Konyushkin, V. A.; Nakladov, A. N.; Kuznetsov, S. V.; Farooq, A.; Gharibzadeh, S.; Paetzold, U. W. Harvesting Sub-Bandgap Photons via upconversion for Perovskite Solar Cells. *ACS Appl. Mater. Interfaces* **2021**, *13* (46), 54874–54883.

(11) Rong, Y.; Hassan, M. M.; Ouyang, Q.; Chen, Q. Lanthanide Ion (Ln^{3+})-based upconversion Sensor for Quantification of Food Contaminants: A Review. *Compr. Rev. Food Sci. Food Saf.* **2021**, *20* (4), 3531–3578.

(12) Gao, G.; Turshatov, A.; Howard, I. A.; Busko, D.; Joseph, R.; Hudry, D.; Richards, B. S. Up-Conversion Fluorescent Labels for Plastic Recycling: A Review. *Adv. Sustain. Syst.* **2017**, *1* (5), 1600033.

(13) *Plastics - the Facts 2022*; ● Plastics Europe. URL: https://plasticseurope.org/knowledge-hub/plastics-the-facts-2022/. Date of access: 31.07.2023.

(14) *EUR-Lex - 52018DC0028 - EN*; EUR-Lex. URL: https://eur-lex.europa.eu/legal-content/EN/TXT/?uri=COM%3A2018%3A28%3AFIN. Date of access: 31.07.2023.

(15) Friedrich, K.; Koinig, G.; Pomberger, R.; Vollprecht, D. Qualitative Analysis of Post-Consumer and Post-Industrial Waste via near-Infrared, Visual and Induction Identification with Experimental Sensor-Based Sorting Setup. *MethodsX* **2022**, *9*, 101686.

(16) Gasde, J.; Woidasky, J.; Moesslein, J.; Lang-Koetz, C. Plastics Recycling with Tracer-Based-Sorting: Challenges of a Potential Radical Technology. *Sustainability* **2021**, *13* (1), 258.

(17) Woidasky, J.; Sander, I.; Schau, A.; Moesslein, J.; Wendler, P.; Wacker, D.; Gao, G.; Kirchenbauer, D.; Kumar, V.; Busko, D. Inorganic Fluorescent Marker Materials for Identification of Post-Consumer Plastic Packaging. *Resour. Conserv. Recycl.* **2020**, *161*, 104976.

(18) Atuchin, V. V.; Aleksandrovsky, A. S.; Chimitova, O. D.; Diao, C.-P.; Gavrilova, T. A.; Kesler, V. G.; Molokeev, M. S.; Krylov, A. S.; Bazarov, B. G.; Bazarova, J. G. Electronic Structure of β-RbSm (MoO 4) 2 and Chemical Bonding in Molybdates. *Dalt. Trans.* **2015**, *44* (4), 1805–1815.

(19) Li, L.; Liu, Y.; Li, R.; Leng, Z.; Gan, S. Tunable Luminescence Properties of the Novel Tm^{3+}-and Dy^{3+}-Codoped LiLa-$(MoO^4)_x(WO_4)_{2-x}$ Phosphors for White Light-Emitting Diodes. *RSC Adv.* **2015**, *5* (10), 7049–7057.

(20) Wang, J.; Luo, L.; Huang, B.; He, J.; Zhang, W.; Zhao, W.; Wang, J. The Preparation and Optical Properties of Novel $LiLa(MoO_4)_2$:Sm^{3+}, Eu^{3+} Red Phosphor. *Materials (Basel).* **2018**, *11* (2), 297.

(21) Chang, Y. C.; Liang, C. H.; Yan, S. A.; Chang, Y. S.Synthesis and Photoluminescence Characteristics of High Color Purity and Brightness $Li_3Ba_2Gd_3(MoO_4)_8$:Eu^{3+} Red Phosphors. *J. Phys. Chem. C* **2010**, *114* (8), 3645–3652.

(22) Armand, P.; Granier, D.; Reibel, C.; Tillard, M. Growth, Crystal Structure, and Properties of the $Li_3Ba_2Ln_3$ $(MoO_4)_8$ (Ln= Er, Tm) Molybdates. *Solid State Sci.* **2022**, *123*, 106796.

(23) García-Cortés, A.; Cascales, C. Crystal Growth and Optical and Spectroscopic Characterization of the Ytterbium-Doped Laser Molybdate Yb– $Li_3Gd_3Ba_2(MoO_4)_8$. *Chem. Mater.* **2008**, *20* (12), 3884–3891.

(24) Klevtsova, R. F.; Vasil'ev, A. D.; Glinskaya, L. A.; Kruglik, A. I.; Kozhevnikova, N. M.; Korsun, V. P. Crystal Structure Investigation of Ternary Molybdates $Li_3Ba_2Ln_3$ $(MoO_4)_3$ (Ln= Gd, Tm). *J. Struct. Chem.* **1992**, *33* (3), 443–447.

(25) Kozhevnikova, N. M.; Kopylova, O. A. Synthesis and X-Ray Diffraction and IR Spectroscopy Studies of Ternary Molybdates $Li_3Ba_2R_3(MoO_4)_8$(R= La-Lu, Y). *Russ. J. Inorg. Chem.* **2011**, *56* (6), 935–938.

(26) García-Cortés, A.; Zaldo, C.; Cascales, C.; Mateos, X.; Petrov, V. Laser Operation of Yb^{3+} in Disordered $Li_{0.75}Gd_{0.75}Ba_{0.5}(MoO_4)_2$ Crystal with Small Quantum Defect. *Opt. Express* **2007**, *15* (26), 18162–18167.

(27) Keil, J.-N.; Paulsen, C.; Rosner, F.; Pöttgen, R.; Jüstel, T. On the Crystal Structure and Optical Spectroscopy of Rare Earth Comprising Quaternary Tungstates $Li_3Ba_2RE_3$ $(WO_4)_8$ (RE= La–Nd, Sm–Ho). *Dalt. Trans.* **2021**, *50* (26), 9225–9235.

(28) Katelnikovas, A.; Plewa, J.; Sakirzanovas, S.; Dutczak, D.; Enseling, D.; Baur, F.; Winkler, H.; Kareiva, A.; Jüstel, T. Synthesis and Optical Properties of $Li_3Ba_2La_3$ $(MoO_4)_8$: Eu^{3+} Powders and Ceramics for PcLEDs. *J. Mater. Chem.* **2012**, *22* (41), 22126–22134.

(29) Hu, J.; Gong, X.; Huang, J.; Chen, Y.; Lin, Y.; Luo, Z.; Huang, Y. Near Ultraviolet Excited Eu^{3+} Doped $Li_3Ba_2La_3(WO_4)_8$ Red

Phosphors for White Light Emitting Diodes. *Opt. Mater. Express* **2016**, *6* (1), 181−190.
(30) Guo, C.; Gao, F.; Liang, L.; Choi, B. C.; Jeong, J.-H. Synthesis, Characterization and Luminescent Properties of Novel Red Emitting Phosphor $Li_3Ba_2Ln_3(MoO_4)_8$: Eu^{3+} (Ln= La, Gd and Y) for White Light-Emitting Diodes. *J. Alloys Compd.* **2009**, *479* (1−2), 607−612.
(31) Song, M.; Wang, G.; Zhang, L.; Lin, Z.; Wang, G. Growth and Spectral Properties of Yb^{3+}-Doped $Li_3Ba_2Y_3(MoO_4)_8$ Crystal. *J. Alloys Compd.* **2009**, *478* (1−2), 423−426.
(32) Song, M.; Wu, M.; Zhou, W.; Zhou, X.; Wei, B.; Wang, G. Growth, Structure and Spectral Properties of Dy^{3+}-Doped $Li_3Ba_2La_3(MoO_4)_8$ Crystal for Potential Use in Solid-State Yellow Lasers. *J. Alloys Compd.* **2014**, *607*, 110−117.
(33) Li, J.; Wang, J.; Zhang, Y.; Zhang, T. Growth, Crystal Structure and Optical Properties of New Laser Crystal $Li_3Ba_2Nd_3$ $(MoO_4)_8$. *J. Cryst. Growth* **2013**, *381*, 61−64.
(34) Krishnan, R.; Menon, S. G.; Poelman, D.; Kroon, R. E.; Swart, H. C. Power-Dependent upconversion Luminescence Properties of Self-Sensitized Er_2WO_6 Phosphor. *Dalt. Trans.* **2021**, *50* (1), 229−239.
(35) Berry, M. T.; May, P. S. Disputed Mechanism for NIR-to-Red upconversion Luminescence in $NaYF_4$: Yb^{3+}, Er^{3+}. *J. Phys. Chem. A* **2015**, *119* (38), 9805−9811.
(36) Würth, C.; Resch-Genger, U. Determination of Photoluminescence Quantum Yields of Scattering Media with an Integrating Sphere: Direct and Indirect Illumination. *Appl. Spectrosc.* **2015**, *69* (6), 749−759.
(37) Zhang, M.; Zheng, W.; Liu, Y.; Huang, P.; Gong, Z.; Wei, J.; Gao, Y.; Zhou, S.; Li, X.; Chen, X. A New Class of Blue-LED-Excitable NIR-II Luminescent Nanoprobes Based on Lanthanide-Doped CaS Nanoparticles. *Angew. Chemie Int. Ed.* **2019**, *58* (28), 9556−9560.
(38) Pei, Y.; Tu, D.; Li, C.; Han, S.; Xie, Z.; Wen, F.; Wang, L.; Chen, X. Boosting Near-Infrared Luminescence of Lanthanide in $Cs_2AgBiCl_6$ Double Perovskites via Breakdown of the Local Site Symmetry. *Angew. Chemie Int. Ed.* **2022**, *61* (30), No. e202205276.
(39) Sun, J.; Zheng, W.; Huang, P.; Zhang, M.; Zhang, W.; Deng, Z.; Yu, S.; Jin, M.; Chen, X. Efficient Near-Infrared Luminescence in Lanthanide-Doped Vacancy-Ordered Double Perovskite Cs_2ZrCl_6 Phosphors via Te^{4+} Sensitization. *Angew. Chemie Int. Ed.* **2022**, *61* (26), No. e202201993.
(40) Lei, X.; Li, R.; Tu, D.; Shang, X.; Liu, Y.; You, W.; Sun, C.; Zhang, F.; Chen, X. Intense Near-Infrared-II Luminescence from $NaCeF_4$: Er/Yb Nanoprobes for in Vitro Bioassay and in Vivo Bioimaging. *Chem. Sci.* **2018**, *9* (20), 4682−4688.
(41) Wang, D.; Wang, D.; Kuzmin, A.; Pliss, A.; Shao, W.; Xia, J.; Qu, J.; Prasad, P. N. ICG-Sensitized $NaYF_4$: Er Nanostructure for Theranostics. *Adv. Opt. Mater.* **2018**, *6* (12), 1701142.
(42) Wang, X.; Yakovliev, A.; Ohulchanskyy, T. Y.; Wu, L.; Zeng, S.; Han, X.; Qu, J.; Chen, G. Efficient Erbium-sensitized Core/Shell Nanocrystals for Short Wave Infrared Bioimaging. *Adv. Opt. Mater.* **2018**, *6* (20), 1800690.
(43) Krishnan, R.; Thirumalai, J.; Kathiravan, A. Luminescence and Magnetic Properties of Novel Nanoparticle-Sheathed 3D Micro-Architectures of $Fe_{0.5}R_{0.5}(MoO_4)_{1.5}$: Ln^{3+}(R= Gd^{3+}, La^{3+}),(Ln= Eu, Tb, Dy) for Bifunctional Application. *Electron. Mater. Lett.* **2015**, *11*, 24−33.
(44) Wilson, L. R.; Richards, B. S. Measurement Method for Photoluminescent Quantum Yields of Fluorescent Organic Dyes in Polymethyl Methacrylate for Luminescent Solar Concentrators. *Appl. Opt.* **2009**, *48* (2), 212−220.
(45) Joseph, R. E.; Jiménez, C.; Hudry, D.; Gao, G.; Busko, D.; Biner, D.; Turshatov, A.; Krämer, K.; Richards, B. S.; Howard, I. A. Critical Power Density: A Metric to Compare the Excitation Power Density Dependence of Photon upconversion in Different Inorganic Host Materials. *J. Phys. Chem. A* **2019**, *123* (31), 6799−6811.